Chemical Science

ROYAL SOCIETY OF CHEMISTRY

EDGE ARTICLE

View Article Online
View Journal | View Issue



Cite this: *Chem. Sci.*, 2026, **17**, 2818

All publication charges for this article have been paid for by the Royal Society of Chemistry

Received 15th October 2025
Accepted 3rd December 2025

DOI: 10.1039/d5sc07981k

rsc.li/chemical-science



# Dual conformational emission and vibrational coherence in a sulfone-embedded narrowband emitter

Simin Jiang,[a] Yanmei He,*[b] Guo-Xi Yang,[a] Tönu Pullerits [b] and Shi-Jian Su *[a]

Organic luminescent narrowband emitters have emerged as promising candidates for wide-color-gamut displays. However, the comprehensive photo-induced structural and vibrational dynamics responsible for the spectral broadening remain poorly understood. In this study, ultrafast spectroscopy is employed to elucidate the excited state dynamics of a sulfone-embedded narrowband emitter, 2tCPD. An intrinsic dual emission, which originates from a reversible conformational transition between boat and chair structures on a timescale of ~100 ps, is revealed. In aromatic toluene solution, the metastable chair conformation is stabilized by forming a sandwich-like toluene–2tCPD–toluene complex through weak π–π interaction, thereby switching the dominant emission to the chair form. Furthermore, the direct observation of coherent oscillations enables the visualization of vibronic coupling in 2tCPD, where the key vibrational mode at 180 $cm^{-1}$ oscillates along the excited-state potential energy surface of the boat conformation. This mode, which involves the bending vibration of sulfone and out-of-plane bending of carbonyl and peripheral phenyl groups, mainly drives the structural reorganization during the electronic transition. These findings provide mechanistic insights into conformation-dependent emission in narrowband emitters and underscore the crucial vibrational information in guiding the molecular design toward high color-purity organic fluorophores.

## Introduction

Thermally activated delayed fluorescence (TADF) emitters have emerged as promising candidates for the next generation organic light-emitting diodes (OLEDs), owing to their capacity of triplet utilization in the absence of heavy metal atoms.[1–5] The ability to harvest triplet excitons, which intrinsically originates from the endothermic upconversion of dark triplet state ($T_1$) to emissive singlet state ($S_1$) *via* the reverse intersystem crossing (RISC) process, has been well documented to correlate with the singlet–triplet splitting energy ($\Delta E_{ST}$), oscillator strength of singlet emission and spin–orbital coupling.[6–10] Recently, insights into molecular design strategies based on the multiple resonance (MR) effect provide TADF-based OLEDs with a compelling pathway toward highly efficient wide-color gamut displays, in which narrowband emission holds key significance.[11–13]

Generally, molecular emission spectrum is primarily determined by its intrinsic chemical structure. In MR emitters, the rigid skeleton and unique alternating distribution of frontier molecular orbitals enable the minimized excited-state nuclear reorganization and vibronic coupling during electronic transition, giving rise to a small molecular geometry displacement and narrowband emission.[11] Subsequent studies revealed that the emission spectra of MR emitters can be further narrowed by incorporating the low-frequency molecular vibrational modes into the MR skeleton such as the twisting of phenyl group[14] or the bending of sulfone group.[15,16] Comprehensive theoretical calculation results elucidated the mechanism of the narrowed emission spectrum, which originates from the weakened contribution of higher-frequency vibration modes to molecular emission. By computing the Franck–Condon factors, the vibrationally resolved electronic spectra could be predicted. However, as the calculations depend on methodological approximations[17] and simplified models of the molecular environment, the resulting vibrationally resolved electronic spectra often deviate from the actual molecular spectra.[18,19] The lack of experimental insights into specific molecular vibrational modes upon electronic transition confines the current interpretations to a theoretical realm and hampers the in-depth understanding of narrowband emission mechanism in MR emitters.

Apart from the chemical structure, the molecular excited state dynamics also contributes to the emission spectrum. For MR emitters, the steric congestion in their polycyclic aromatic skeleton results in a nonplanar contorted geometry. Such the contorted structure endows these polycyclic aromatic

[a]*Guangdong Basic Research Center of Excellence for Energy and Information Polymer Materials, State Key Laboratory of Luminescent Materials and Devices, South China University of Technology, Wushan Road 381, Guangzhou 510640, P. R. China. E-mail: mssjsu@scut.edu.cn*

[b]*Division of Chemical Physics and NanoLund, Lund University, P. O. Box 124, Lund 22100, Sweden. E-mail: yanmei.he@chemphys.lu.se*

compounds with unique and complicated excited state dynamics,[20] which, however, introduces an inherent risk of multimode luminescence. For instance, dual emission, arising from simultaneous fluorescence and phosphorescence[21] or radiative combination of a localized excited state and a charge transfer state,[22] represents a major source of spectral broadening in MR emitters. Besides, the excited state planarization process initiated by the nuclear motions of contorted molecules would sometimes induce multi-step structural relaxations or isomerization on their $S_1$ potential energy surface (PES), leading to intrinsic multi-conformational emission and spectral broadening.[23–26] So far, a few studies have revealed the involvement of excited state planarization in MR emitters,[27,28] whereas the correlation between excited state structural dynamics and molecular narrowband emission is still poorly understood. Despite the flourishing of diverse molecular designs[29–31] and fascinating applications[32–35] in MR molecules, there remains a scarcity of experimental studies that provide a molecular-level view of the impact of structural and vibrational dynamics on the narrowband emission of MR emitters. A comprehensive understanding of the excited state structural and vibrational dynamics is therefore essential to unlock the narrowband emission mechanism and facilitate the further development of MR materials.

In this study, we investigated the interplay between solvents and conformational dynamics in the molecular emission of a sulfone-embedded narrowband emitter 2tCPD,[16] aiming to gain deeper insight into its fundamental structural and nuclear dynamics. Combining femtosecond transient absorption spectroscopy (fs-TA) measurements with theoretical calculation results, we revealed an intrinsic dual emission in 2tCPD. The dual emission, observed in both the aromatic solvent toluene and the non-aromatic solvent dichloromethane (DCM), originates from the mutual radiative combination of the so-called boat and chair conformations. In DCM, molecular emission is primarily from the boat form, as it is the most energetically stable conformation. In contrast, the metastable chair conformation is stabilized in toluene by forming a toluene–2tCPD–toluene complex, leading to a prominently enhanced emission from the chair conformation. Furthermore, the wavepacket motion along the $S_1$ PES of the boat conformation was studied by precisely analyzing the coherent oscillatory dynamics. This signal of wavepacket dynamics, which encodes the superposition of Franck-Condon active vibrational modes, offers a promising pathway to investigate the molecular vibrational motions induced by the electronic excitation.[36–39] By performing the Fourier transform of the residual TA spectrum, a dominant vibrational mode of 180 $cm^{-1}$ in the low-frequency region was uncovered. The mode is assigned to the bending vibrations of sulfone groups and out-of-plane bending of carbonyl and phenyl groups, which together account for the primary structural reorganization during the ground state ($S_0$) → $S_1$ transition. This comprehensive exploration on the influence of structural dynamics and vibrational coherence in narrowband emission provides valuable guidance for ongoing computational and experimental efforts towards the rational design and deeper understanding of narrowband MR emitters.

## Results and discussion

Ultraviolet-visible (UV-vis) absorption and photoluminescence (PL) spectra of 2tCPD were measured in the representative aromatic solvent toluene and the non-aromatic solvent DCM, respectively. As shown in Fig. 1a, the absorption of 2tCPD in toluene is identical to that in DCM, exhibiting a well-resolved π–π* transition ($S_0$ → $S_1$) in the 425–550 nm region and the high-energy π–π* and/or n–π* transition below 400 nm.[15,40] However, their emission behaves quite differently as evidenced in the PL spectra (Fig. 1b). In DCM, 2tCPD shows a nearly mirrored PL emission (centered at 533 nm) relative to the absorption band. While a new dominant emission band centered at ~560 nm is observed in toluene. This abnormal PL emission is further replicated in other aromatic solvents despite the variations in intensity (Fig. S1), which indicates the presence of an unidentified process in aromatic solvents. To exclude the possibility of aggregate emission, we investigated the time-resolved emission spectra (TRES) of 2tCPD in toluene and the tetrahydrofuran (THF)/water mixture with one volume percent of THF, respectively. Compared to a time-evolved red-shifted emission band beyond 600 nm in the THF/water mixture, the spectral evolution in toluene is nearly negligible on the nanosecond timescale (Fig. 1c and S2). These results suggest that the abnormal emission of 2tCPD in toluene is indeed driven by its intrinsic excited state dynamics on a much shorter timescale than nanosecond. Probably due to the relatively large $\Delta E_{ST}$ (0.25 eV, estimated in hexane[16]), we failed to detect the long-lived delayed fluorescence under ambient conditions. The lifetimes of 2tCPD in toluene and DCM are found to be 7.5 and 6.5 ns, respectively (Fig. 1d).

To gain a comprehensive understanding of the solvent-response mechanism and excited state dynamics, fs-TA of 2tCPD in toluene and DCM was carried out, using pump light centered at 510 nm and super continuum white light for the probe (time resolution at the sample position: ~100 fs). As shown in Fig. 2a and b, the TA spectrum in toluene reveals a pronounced negative signal in the range of 450–540 nm with two distinct peaks centered at 490 and 523 nm. This is assigned to the ground-state bleaching (GSB) signal, which is consistent with the steady-state absorption spectrum (Fig. 1a). Considering the minimized Stokes shift of the narrowband emitter, the stimulated emission (SE) feature also contributes the negative signal. A broad excited state absorption (ESA) in the 400–450 nm and 540–1000 nm regions is resolved. During the first 3 ps, the TA spectral evolution involves an indistinct SE development with a slight red-shift of the bleach (Fig. S3a). Considering the higher-energy excitation (510 nm, 2.43 eV) than the 0–0 transition absorption (peak at 520 nm, 2.38 eV), the excited state cooling process occurs before reaching the equilibrium position of the PES. Interestingly, a well-resolved oscillatory kinetic signal at ~540 nm was observed during the first 3 ps (Fig. S3b), as a result of coupling between electronic and vibrational degrees of freedom.[41] The coherent oscillations will be discussed later in detail. From 30 to 300 ps, the broad ESA signal evolves into a more complex shape: the ESA band in the range of 600–620 nm changes to two new ESA bands ranging from 565–

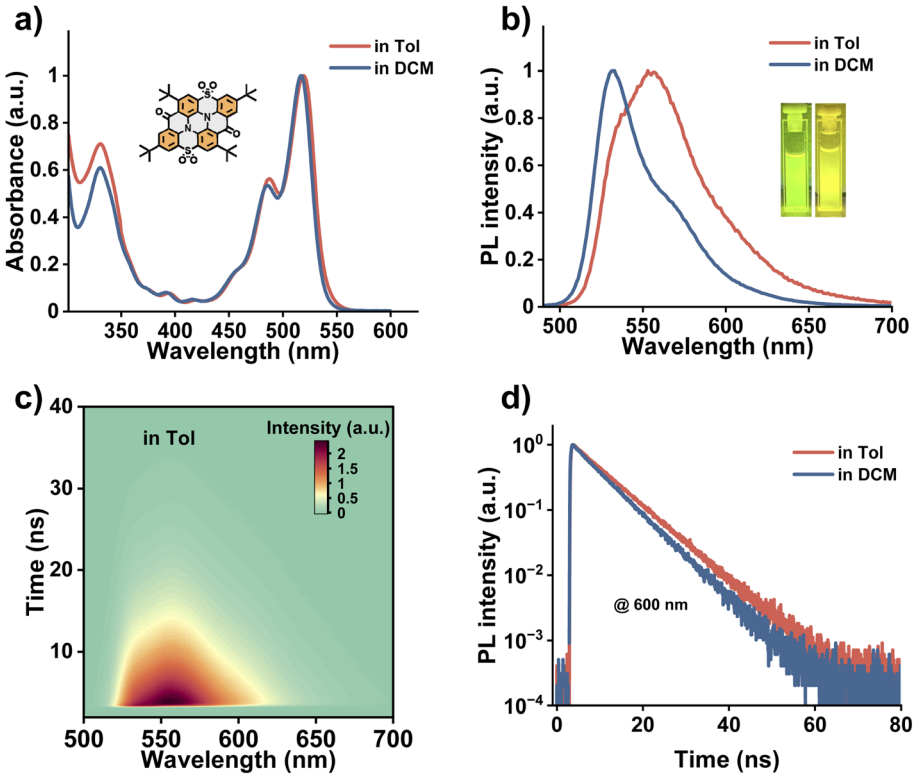


Fig. 1 The basic photophysical characterization of 2tCPD in toluene and DCM. (a) UV-vis absorption spectra of 2tCPD in toluene and DCM (inset: chemical structure of 2tCPD). (b) PL spectra of 2tCPD in toluene and DCM (inset: emission photographs in cuvettes, left: in DCM; right: in toluene). (c) TRES of 2tCPD in toluene. (d) Fluorescence lifetime in toluene and DCM traced at 600 nm, under 375 nm excitation.

595 nm and 630–660 nm (Fig. 2b). Besides, a distinct blue shift in the 530–550 nm region accompanies the spectral evolution. The concurrent decay and rising time traces at 610 and 585 nm (~100 ps) also support the observation (Fig. S3d), showing that $S_1$ transforms to a new state (temporally named M) on the timescale of 120 ps. The M state most likely maintains the singlet character, since it shows the similar main ESA band at ~911 nm. After 500 ps, the amplitude of the ESA band continuously decreases along with the peaks shifting to 600, 700 and 880 nm (Fig. S3c). Also, the GSB signal decays.

To understand the excited state dynamics, the global analysis (GLA) was performed based on a sequential model using the singular value decomposition (SVD) method. We obtained four components with lifetimes of 1.3 ps, 122 ps, 8.7 ns and >10 ns, respectively. The fastest 1.3 ps component is assigned to vibrational relaxation, while the 122 ps component corresponds to the M state formation. Considering the similar time constant to that of the fluorescence lifetime (7.5 ns), we assign the 8.7 ns component to the decay of the emissive singlet state, in which two competing pathways are involved: radiative recombination to the ground state and intersystem crossing (ISC). The remaining excitons undergo the ISC process to the $T_1$ state, due to the $\Delta E_{ST}$ of ~0.25 eV.[16] The longest component (>10 ns) is attributed to the deactivation of the $T_1$ state.

Although the above analysis provides a comprehensive insight into the excited state dynamics of 2tCPD in toluene, the nature of the M state needs further explanation. Given that the accompanying spectral shift in the 540–560 nm range coincides with the region of the abnormal emission observed in the steady-state PL (Fig. 1b), we sought to establish a connection between these two observations. In other words, we hypothesize that the emission at 560 nm originates from the radiative decay of the M state. To further verify this hypothesis, we measured time-resolved PL spectra on the picosecond timescale using streak camera (excitation: 400 nm; time resolution: 2 ps). In Fig. 2d, the 520 nm emission shows a fast decay before 300 ps, which occurs simultaneously with the rise of the PL at 570 nm. By performing exponential fitting, a fast decay component with a lifetime of 109 ps and a long component with a lifetime of >2 ns were obtained. The 109 ps component aligns well with the time constant (122 ps) obtained from TA measurement. Therefore, we conclude that the abnormal emission comes from the M state.

In comparison, the fs-TA measurements of 2tCPD in non-aromatic DCM were carried out, see Fig. S4. The GLA results also give four components: $\tau_1 \sim 630$ fs, $\tau_2 \sim 108$ ps, $\tau_3 \sim 5.8$ ns, and $\tau_4 > 10$ ns. The first component is similarly attributed to the vibrational relaxation, which is notably faster than that in toluene due to the relatively larger solvent polarity. The shorter lifetime of 5.8 ns is in line with the shorter PL lifetime (Fig. 1d). It is noteworthy that a similar transition from $S_1$ to the possible M state was also tracked within ~108 ps, which is supported by the similar trend in kinetics despite the smaller changes in amplitude (Fig. S4d and e). The transition is further supported by the streak camera measurements with synchronous decay and rise of kinetics at 520 and 570 nm (Fig. S4f). These results imply that the transition from $S_1$ to the possible M state is an

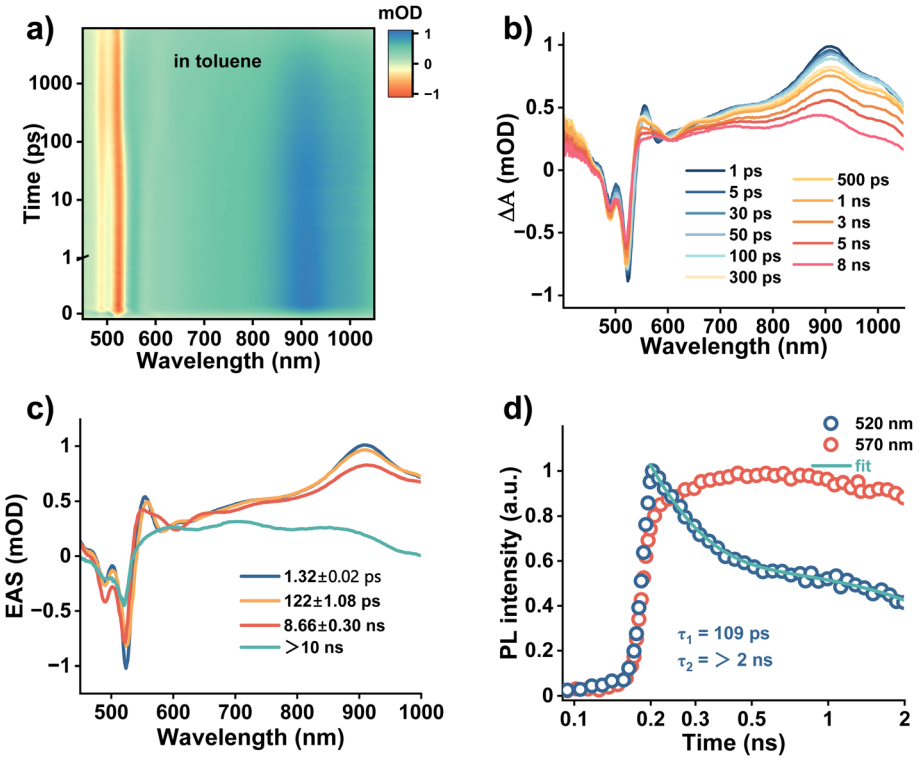


Fig. 2 Ultrafast excited state dynamics exploration of 2tCPD in toluene. (a) Pseudocolor representation of fs-TA spectra of 2tCPD in toluene. (b) The fs-TA spectra of 2tCPD as a function of time delay. (c) The EAS spectra obtained from global fitting. (d) Kinetic curves traced at 520 and 570 nm using the streak camera.

intrinsic feature of the molecular system, while it might be reinforced in toluene, suggesting a potential interaction between the aromatic solvent and emissive molecules.

To identify the possible interaction, single crystals of 2tCPD were cultivated in chloroform (due to the higher boiling point compared to DCM) and toluene, named as 2tCPD_TCM (CCDC number: 2224085) and 2tCPD_Tol (CCDC number: 2452457), respectively. For 2tCPD_TCM, the molecule in crystal exhibits a saddle-shaped geometry, which is manifested as a boat-type conformation with the two sulfone groups on the same side of the main molecular plane and the two carbonyl groups on the other side (Fig. S5a). However, in the 2tCPD_Tol crystal, toluene molecules contribute to the crystal structure by forming a sandwich-like toluene–2tCPD–toluene complex through π–π interaction (Fig. S5b). Besides, the molecular conformation changes to the chair-type with the groups (sulfone and carbonyl) distributed on both sides of the main molecular plane. The remarkable geometry alteration indicates a potential correlation between the molecular conformation and excited state dynamics.

To reveal this relationship between molecular geometry and excited state dynamics, theoretical calculations[42] based on density functional theory (DFT) and time-dependent DFT (TD-DFT) were carried out to optimize the $S_0$ and $S_1$ geometries of the boat and chair conformations (initial structures were extracted from the crystals). As shown in Fig. 3a, the boat conformation of 2tCPD was estimated to be the more stable geometry in the $S_0$ state with an energy 0.155 eV lower than that of the chair conformation, which accounts for the observed boat structure in 2tCPD_TCM crystal. Similarly, the optimized $S_1$ energy of the boat conformation is 0.08 eV lower than that of the chair conformation. Therefore, the main excited-state dynamics of 2tCPD in DCM could be explicitly attributed to the electronic transition between $S_0$ and $S_1$ in the boat conformation, as it is also supported by the close agreement between the theoretically estimated fluorescence (2.36 eV) and the experimentally observed emission peak at 533 nm (2.32 eV). Given the slightly lower energy of the estimated emission of the chair conformation (2.29 eV), we suggest that the $S_1$ of chair conformation corresponds to the M state. The transition from $S_1$ to M involves the conformational change from boat to chair. To further elucidate the scenario, we performed a flexible two-dimensional PES scan from the optimized boat to chair geometry by altering the dihedral angles between the main molecular plane and the carbonyl and sulfone groups (Fig. S6). As shown in Fig. 3a and b, in the $S_0$ state, the energy barrier for the boat-to-chair conformation was estimated to ~0.22 eV. Considering the prerequisite for the RISC pathway in TADF materials with a typical requirement of $\Delta E_{ST} \leq 0.25$ eV,[5,43,44] the conformational transformation is expected to occur at room temperature by utilizing ambient thermal energy to overcome the barrier. However, due to the higher-energy metastable geometry of the chair conformation and the shallow detrapping energy barrier (~0.065 eV), the 2tCPD molecules are unable to permanently remain in the chair conformation. Therefore, in the $S_0$ state, a reversible boat-to-chair conformational transformation occurs, while the 2tCPD molecules dominantly remain in the boat form owing to its more energy-stable geometry. Upon photoexcitation, the 2tCPD molecules in the boat

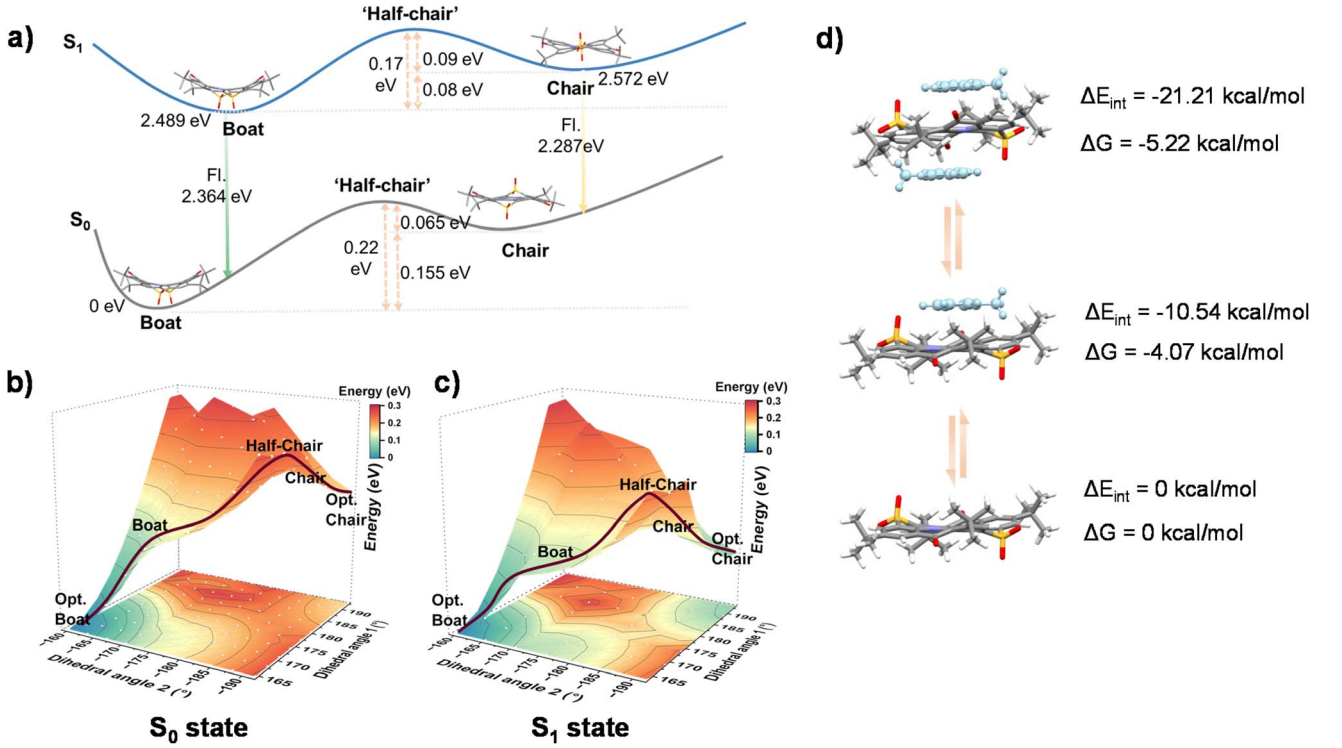


Fig. 3 Theoretical calculation results for the 2tCPD molecule. (a) The calculated energy levels of boat and chair conformations in $S_0$ and $S_1$ states. (b) Two-dimensional potential energy surface in the $S_0$ state. (c) Two-dimensional potential energy surface in the $S_1$ state. (d) Interaction energy of the complex.

conformation are excited to their excited state, followed by fast vibrational relaxation to the minimum PES of the boat conformation. In the $S_1$ state, the energy barrier from boat to chair is reduced to ~0.17 eV and the reverse chair-to-boat barrier is slightly increased to ~0.09 eV. This energy level arrangement favors the increased stability for the chair conformation. In other words, the population of chair conformations is increased under dynamic equilibrium, compared to that in the $S_0$ state. Therefore, it is reasonable to observe emission from the $S_1$ state of the chair conformation. However, owing to the intrinsic metastable nature of the chair conformation and the relatively small energy barrier, the population of chair conformations should remain quite low under dynamic equilibrium, which well explains the small intensity changes in TA measurement (Fig. S4e) and streak camera measurements (Fig. S4f).

While in toluene solution, the 2tCPD molecules are induced to assemble with toluene molecules *via* π–π interaction, forming a sandwich-like toluene–2tCPD–toluene complex. Due to the saddle-shape geometry of the boat conformation, which features a relatively twisted molecular skeleton and bulky steric hindrance from sulfone and carbonyl groups, it is difficult for the boat conformation to establish such short-distance π–π interactions with two toluene molecules. Hence, we propose that the sandwich-like complex is formed *via* the interaction between toluene and the chair conformation. Once the molecule is confined within the sandwich cage, the conformational conversion from the chair-type to the boat-type will be greatly suppressed. As a result, the population of the chair conformation is significantly enhanced, which accounts for the pronounced PL emission at 560 nm in toluene solution. Due to the inherent wide gap of the toluene molecule, the emission behavior of the complex is considered to remain nearly identical to that of the isolated chair conformation. As shown in Fig. S7, the frontier molecular orbitals of the sandwich-like complex are still localized on the 2tCPD molecule. The calculated fluorescence energy (2.192 eV) is slightly lower than that of the isolated 2tCPD molecule, which is probably related to the weak conjugation through space with toluene. Subsequently, the interaction energy ($\Delta E_{int}$) and Gibbs free energy ($\Delta G$) were calculated to estimate the stability of the complex (Fig. 3d). Probably due to the short conjugation length of the toluene molecule, the interaction between toluene molecules and 2tCPD is relatively weak.[45,46] In the solution phase, molecular thermal motion and solvent effects can significantly disrupt the stability of the complex, potentially leading to its dissociation.[47] Therefore, a dynamic equilibrium between complex formation and dissociation is expected to exist in the $S_1$ state. Upon complex dissociation, the metastable chair conformation converts into the energetically favorable boat conformation. Consequently, dual emission originating from both the boat conformation and the complex is verified in toluene solution. Upon relaxation to the $S_0$ state, a similar conformational equilibrium exists. However, due to the larger energy barrier for the boat-to-chair transition, the majority of molecules remain in the boat conformation, with only a small fraction adopting the chair form in the complex.

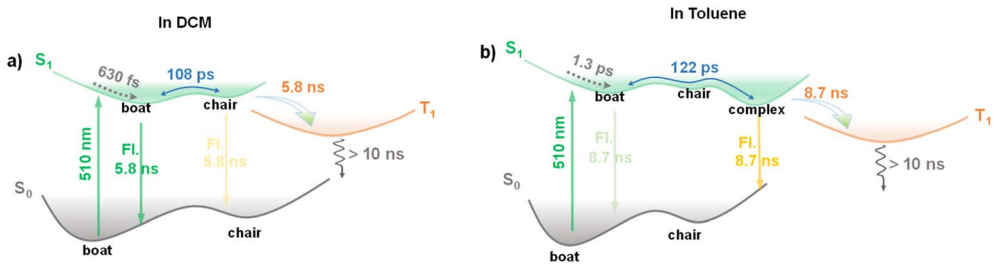


Fig. 4 Schematic illustration of the excited-state dynamics of 2tCPD in (a) DCM and (b) toluene.

Based on the above discussion, we now conclude that the $S_1$ state of the chair conformation corresponds to the M state derived from the GLA results in TA measurements, and the electronic transition from $S_1$ to M involves the conformational change from boat-type to chair-type. The schematic excited-state dynamics of 2tCPD in DCM and toluene are depicted in Fig. 4. In DCM solution, the 2tCPD molecule in the boat conformation is excited to its high-energy $S_1$ state upon 510 nm excitation. The hot excited state undergoes ultrafast vibrational relaxation to its lowest $S_1$ state within 630 fs, followed by a reversible conformational conversion between boat and chair forms with a time scale of 108 ps. The decay lifetime of the $S_1$ state is around 5.8 ns, during which approximately 79% of excitons undergo radiative decay predominantly from the minimum PES of the boat conformation, accompanied by a weak emission from the chair conformation. By estimating the emission band, the ratio of boat and chair forms contributing to emission is approximately determined to be 0.22 : 0.78. The remaining ~21% excitons transition to the $T_1$ state *via* the ISC process and are eventually dissipated by non-radiative recombination with a lifetime of >10 ns. The excited state dynamics of 2tCPD in toluene are similar to those observed in DCM. However, because of the presence of the toluene–2tCPD–toluene complex which stabilizes the chair conformation, the radiative decay predominantly originates from the complex (Fig. 4b).

As mentioned above (Fig. S3c and S4c), a striking oscillatory signal was observed in both DCM and toluene. The oscillatory signal, which encodes the information about wavepacket dynamics with a superposition of Franck–Condon active vibrational modes, provides an opportunity to investigate vibronic coupling. Given the well-documented intrinsic correlation between vibronic coupling and narrowband emission, such insights can deepen the understanding of narrowband emission in MR emitters. The coherent oscillation signals were easily reproduced as shown in Fig. 5a. The detection time window was designed to be 4 ps with a time step of 25 fs, enabling the analysis of well-resolved vibrational wavepackets. The beating maps were obtained by removing the population dynamics. By performing the Fourier transform to the beating map, we obtained the vibrational mode frequencies. As shown in Fig. 5c–e, the frequencies of 10, 134, 180, and 223 $cm^{-1}$ were clearly identified across the SE and ESA bands, with the 180 $cm^{-1}$ frequency showing the strongest amplitude. When the wavepacket is generated by an ultrafast pulse laser, it oscillates with several representative modes along the PES of the particular electronic state.[48] During the wavepacket motion, a phase flip (also called the node) occurs at a certain probe wavelength, which represents the minimum of the PES characterized by the zero amplitude of oscillation. As shown in Fig. 5b, a distinct node was observed at ~557 nm. In addition, there seems to be a blurred node that appeared around 530 nm. While interfered by the incident pulse artifacts in the region of 510–525 nm, it cannot be well identified. For this purpose, we repeated the TA measurement and confirmed the presence of the node at 530 nm by carefully eliminating the interference of the pump pulse (Fig. S8). This probe wavelength (530 nm) is slightly blue-shifted by 3 nm relative to the fluorescence peak at 533 nm observed in the steady-state PL spectrum, which is most likely attributed to an increased energy gap between the $S_0$ and $S_1$ state due to the vibrational excitations in the $S_1$ state.[36] Besides, the observed node around 557 nm also supports the interpretation, as the signal primarily originates from the ESA (might be superimposed with the SE signal) in the $S_1$ state. Due to the bright emission and slow non-radiative process of 2tCPD, we infer weak electronic coupling between $S_1$ and $S_0$ states and exclude the involvement of a conical intersection. Thus, the wavepacket remains on the $S_1$ state. Meanwhile, as demonstrated above, the wavepacket is generated by projecting the ground state of the boat conformation to the excited state. The timescale of conformational conversion in the excited state is two orders of magnitude longer than the coherent nuclear motions (Fig. S10 and Table S1). Therefore, the wavepacket remains confined to other vibrational degrees of freedom within the $S_1$ PES of the boat conformation, without the involvement of the slow boat-to-chair conversion coordinate. Owing to the same origin of the excited state dynamics both in DCM and toluene, the vibrational dynamics of 2tCPD in toluene is almost identical to that in DCM, with similar oscillatory signals and analyzed frequencies (Fig. S9).

As a typical MR emitter, 2tCPD presents intrinsic narrowband emission, in which the vibronic coupling plays an important role. In these sulfone-based narrowband emitters, precise modulation of vibronic coupling by incorporating the low-frequency vibrational modes of sulfone groups has been well documented as an effective pathway to reconstruct the molecular geometric arrangement and suppress bond length variation during electronic transition. As a consequence, the fine vibrational peak of emission contributed by the 0–1 transition can be correspondingly suppressed.[16] The observed wavepackets are therefore expected to underline the role of sulfone groups from the experimental insight, as the analyzed Franck–Condon active vibrational modes in the low-frequency region mainly contribute to structural reorganization during the $S_0 \rightarrow S_1$ transition (Fig. 5f). To identify the specific molecular vibrations involved in the wavepacket motion,

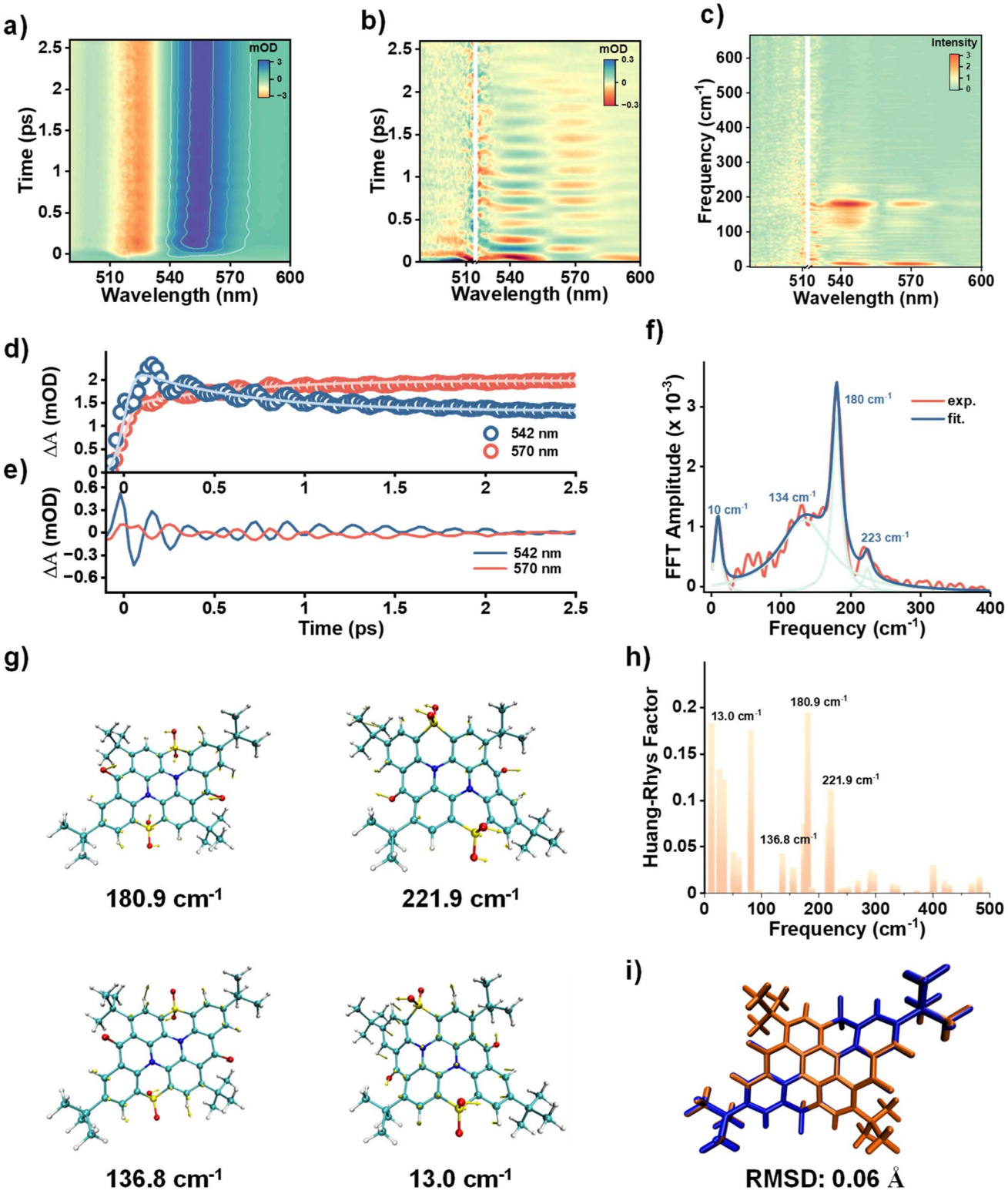


Fig. 5 Coherent wavepacket dynamics of 2tCPD in DCM and calculated molecular vibrational modes and Huang–Rhys factors. (a) fs-TA spectra of 2tCPD in DCM within 2.5 ps. (b) Beating map after subtracting population dynamics. (c) Oscillatory frequencies obtained from Fourier transformation of Fig. 5b. (d) Kinetics and (e) Oscillatory signals probed at 542 and 570 nm. (f) Oscillatory frequencies extracted at 542 nm. (g) Illustration of the representative vibration modes by theoretical calculations. (h) Calculated Huang–Rhys factor from the $S_0$ to $S_1$ transition below 500 $cm^{-1}$. (i) Root-Mean-Square Deviation (RMSD) of the optimized $S_0$ geometry (blue color) and $S_1$ geometry (orange color).

the frequency analysis of 2tCPD was performed based on the optimized boat geometry in the $S_1$ state. These primary observed vibrations are assignable to the calculated modes at 13.0, 136.8, 180.9, and 221.9 $cm^{-1}$, respectively (Fig. 5g). Vibrations of the peripheral non-conjugated *tert*-butyl groups were omitted due to their negligible contribution to the molecular emission. For the vibration at 180 $cm^{-1}$ (180.9 $cm^{-1}$ calculated) with the highest amplitude, the molecular motion involves the collective vibrations of the sulfone, carbonyl and peripheral phenyl groups. Specifically, this mode corresponds to the bending vibration of sulfone (wagging or rocking) along with the out-of-plane bending vibration of phenyl groups and carbonyl groups. Similar vibrational patterns involving the sulfone and phenyl groups are also identified in the modes at 13.0, 136.8 and 221.9 $cm^{-1}$. To explore the relationship between these vibrational modes and structural reorganization, Huang–Rays factors (HRfs) for the modes in the $S_0 \rightarrow S_1$ transition were computed. In line with the experimental observations, the vibrational mode at 180.9 $cm^{-1}$ shows the largest HRf (Fig. 5h). Besides, the vibrational modes at 13.0, 136.8 and 221.9 $cm^{-1}$ also have significant HRfs. As shown in Fig. 5i, the major structural change during the $S_0 \rightarrow S_1$ transition is localized on the peripheral phenyl and sulfone groups, aligning well with the direction of the above-mentioned vibrational modes. This further supports their dominant contribution to structural reorganization. Overall, the experimentally observed Franck–Condon active vibrational modes are well in line with the theoretically computed vibrational modes that greatly contribute to the HRf, highlighting and visualizing the key geometry changes occurring along the specific vibration modes during the $S_0 \rightarrow S_1$ transition.

## Conclusions

In summary, we gained a comprehensive understanding of the excited state structural dynamics and vibrational coherence of the sulfone-embedded narrowband emitter 2tCPD by performing ultrafast spectroscopic investigation of its photophysical processes. By integrating the experimental observations and computational analyses, an intrinsic dual emission, which originates from the radiative recombination of the boat and chair conformation, was identified in both the non-aromatic solvent DCM and the aromatic solvent toluene. In DCM, owing to the global minimum energy of the boat conformation the emission primarily arises from this form. In contrast, by stabilizing the metastable chair conformation *via* forming a toluene–2tCPD–toulene complex, the dominant emission of 2tCPD is switched to the chair in the complex. Naturally, the comparable dual emission pathways lead to significant spectral broadening, which is detrimental to achieving narrowband emission. Our investigation of the excited-state structural dynamics reveals the intrinsic origin of the dual emission and provides a new design perspective for narrowband emitters: minimizing or suppressing conformational changes in the excited state might effectively reinforce the narrowband emission nature. Moreover, the investigation of vibrational coherence reveals the wavepacket motion in the excited state of the boat conformation. The identified vibrational modes at 10, 134, 180 and 223 $cm^{-1}$, primarily involving in the bending of sulfone groups and out-of-plane bending of phenyl groups, are in good agreement with the theoretical calculation results which contribute to the large HRf and structural reorganization during the $S_0 \rightarrow S_1$ transition. These findings provide a detailed depiction of the photophysical processes in MR narrowband emitters and deepen our understanding of intrinsic excited state dynamics in such materials. Furthermore, the experimentally observed vibrational coherence offers critical insight into the key molecular motions during electronic state transitions, providing valuable guidance for the molecular design of next-generation narrowband emitters.

## Author contributions

S. -J. Su initiated and designed the project. Supervision of the research was provided by S. -J. Su and T. Pullerits. Y. He performed the femtosecond transient absorption experiments and conducted the corresponding data analysis. S. Jiang performed the steady state photophysical measurements, single crystal and theoretical calculations. G. -X. Yang contributed to part of the theoretical calculations. The initial draft of the manuscript was prepared by S. Jiang and Y. He. All authors participated in the discussion and revision of the manuscript.

## Conflicts of interest

There are no conflicts to declare.

## Data availability

The data supporting this article have been included as part of the supplementary information (SI). Supplementary information is available. See DOI: https://doi.org/10.1039/d5sc07981k.

CCDC 2224085 and 2452457 contain the supplementary crystallographic data for this paper.[49]

## Acknowledgements

The authors greatly appreciate the financial support from the National Key R&D Research and Development Program of China (no. 2024YFB3612100) and the National Natural Science Foundation of China (project nos. 52273179 and U23A20594). YH acknowledges the support from the Royal Physiographic Society of Lund. The computations were enabled by resources provided by LUNARC, the Centre for Scientific and Technical Computing at Lund University (project LU 2025/17-23 and 2024/17-22). TP acknowledges support from the Swedish Foundation of Strategic Research (IS24-0005), the Swedish Energy Agency (50709-1), the Olle Engkvists Foundation (235-0422) and the Swedish Research Council (2021-05207).

## References

1 H. Uoyama, K. Goushi, K. Shizu, H. Nomura and C. Adachi, *Nature*, 2012, **492**, 234–238.
2 S. Diesing, L. Zhang, E. Zysman-Colman and I. D. W. Samuel, *Nature*, 2024, **627**, 747–753.

3 H. Noda, X.-K. Chen, H. Nakanotani, T. Hosokai, M. Miyajima, N. Notsuka, Y. Kashima, J.-L. Brédas and C. Adachi, *Nat. Mater.*, 2019, **18**, 1084–1090.
4 D.-H. Kim, A. D'aléo, X.-K. Chen, A. D. S. Sandanayaka, D. Yao, L. Zhao, T. Komino, E. Zaborova, G. Canard, Y. Tsuchiya, E. Choi, J. W. Wu, F. Fages, J.-L. Brédas, J.-C. Ribierre and C. Adachi, *Nat. Photonics*, 2018, **12**, 98–104.
5 Y. Tsuchiya, K. Mizukoshi, M. Saigo, T. Ryu, K. Kusuhara, K. Miyata, K. Onda and C. Adachi, *Nat. Commun.*, 2025, **16**, 4815.
6 H. S. Kim, S. H. Lee, S. Yoo and C. Adachi, *Nat. Commun.*, 2024, **15**, 2267.
7 M. K. Etherington, J. Gibson, H. F. Higginbotham, T. J. Penfold and A. P. Monkman, *Nat. Commun.*, 2016, **7**, 13680.
8 P. Li, Z. Chen, M. Y. Leung, S. L. Lai, S. C. Cheng, W. K. Kwok, C. C. Ko, M. Y. Chan and V. W. Yam, *J. Am. Chem. Soc.*, 2025, **147**, 12092–12104.
9 G. Chen, J. R. Swartzfager and J. B. Asbury, *J. Am. Chem. Soc.*, 2023, **145**, 25495–25504.
10 P. Tao, J. Jin, X. Zheng, Y.-J. Pu and W.-Y. Wong, *Matter*, 2025, **8**, 102142.
11 Y. Kondo, K. Yoshiura, S. Kitera, H. Nishi, S. Oda, H. Gotoh, Y. Sasada, M. Yanai and T. Hatakeyama, *Nat. Photonics*, 2019, **13**, 678–682.
12 M. Mamada, M. Hayakawa, J. Ochi and T. Hatakeyama, *Chem. Soc. Rev.*, 2024, **53**, 1624–1692.
13 X. Wu, S. Ni, C. H. Wang, W. Zhu and P. T. Chou, *Chem. Rev.*, 2025, **125**, 6685–6752.
14 X. Qiu, G. Tian, C. Lin, Y. Pan, X. Ye, B. Wang, D. Ma, D. Hu, Y. Luo and Y. Ma, *Adv. Opt. Mater.*, 2020, **9**, 2001845.
15 S. Jiang, D. Liu, Z. Chen, Z. Yang, Y. He, G. X. Yang, D. Li and S. J. Su, *Adv. Funct. Mater.*, 2024, **34**, 2316355.
16 S. Jiang, Y. Yu, D. Li, Z. Chen, Y. He, M. Li, G.-X. Yang, W. Qiu, Z. Yang, Y. Gan, J. Lin, Y. Ma and S.-J. Su, *Angew. Chem., Int. Ed.*, 2023, **62**, e202218892.
17 F. Santoro, A. Lami, R. Improta, J. Bloino and V. Barone, *J. Chem. Phys.*, 2008, **128**, 224311.
18 D. Wan, J. Zhou, Y. Yang, G. Meng, D. Zhang, L. Duan and J. Ding, *Adv. Mater.*, 2024, **36**, 2409706.
19 S. Song, S. Feng, L. Wang, J. Jun, B. Milian-Medina, R. Wannemacher, J. Lee, M. S. Kwon and J. Gierschner, *Adv. Mater.*, 2024, **36**, 2404388.
20 Y. Gu, V. Vega-Mayoral, S. Garcia-Orrit, D. Schollmeyer, A. Narita, J. Cabanillas-Gonzalez, Z. Qiu and K. Mullen, *Angew. Chem., Int. Ed.*, 2022, **61**, e202201088.
21 B. Du, Y. Wu, X. Wang, H. Tian, S. Shao and L. Wang, *Chem. Sci.*, 2024, **15**, 19432–19442.
22 Y. Chang, Y. Wu, X. Wang, W. Li, Q. Yang, S. Wang, S. Shao and L. Wang, *Chem. Eng. J.*, 2023, **451**, 138545.
23 X. Jin, S. Guo, X. Wang, M. Cong, J. Chen, Z. Zhang, J. Su, D. H. Qu and H. Tian, *Angew. Chem., Int. Ed.*, 2023, **62**, e202305572.
24 Z. Zhang, Y. S. Wu, K. C. Tang, C. L. Chen, J. W. Ho, J. Su, H. Tian and P. T. Chou, *J. Am. Chem. Soc.*, 2015, **137**, 8509–8520.
25 G. Xia, L. Si and H. Wang, *Mater. Today Chem.*, 2023, **30**, 101596.
26 C. Yuan, S. Saito, C. Camacho, S. Irle, I. Hisaki and S. Yamaguchi, *J. Am. Chem. Soc.*, 2013, **135**, 8842–8845.
27 Y. Gao, Y. Wang, Z. Guo, Y. Wan, C. Li, B. Yang, W. Yang and X. Ma, *J. Phys. Chem. B*, 2022, **126**, 2729–2739.
28 Y. Liu, W. Chen, Z. Mahmood, X. He, W. Li, H. Liang, M. D. Li, Y. Huo and S. Ji, *Adv. Funct. Mater.*, 2025, e08754.
29 F. Zhang, V. Brancaccio, F. Saal, U. Deori, K. Radacki, H. Braunschweig, P. Rajamalli and P. Ravat, *J. Am. Chem. Soc.*, 2024, **146**, 29782–29791.
30 W. Yuan, Q. Jin, M. Du, L. Duan and Y. Zhang, *Adv. Mater.*, 2024, **36**, 2410096.
31 Z. Yang, D. Liu, X. Cheng, T. Wang, Z. Li, G. X. Yang, Z. Chen, J. Hu, Y. Fu, X. Nie, Y. Ren, Y. Zeng, Y. Chen, K. Liu, M. Li and S. J. Su, *Angew. Chem., Int. Ed.*, 2025, **64**, e202423602.
32 T. Tsagaantsooj, X. Tang, T. Zhang, Y. T. Lee, R. Walia, X. K. Chen and C. Adachi, *Angew. Chem., Int. Ed.*, 2025, **64**, e202504652.
33 C. Si, W. L. Primrose, Y. Xu, Z. M. Hudson and E. Zysman-Colman, *Adv. Opt. Mater.*, 2024, **13**, 2402576.
34 X. Cao, K. Pan, J. Miao, X. Lv, Z. Huang, F. Ni, X. Yin, Y. Wei and C. Yang, *J. Am. Chem. Soc.*, 2022, **144**, 22976–22984.
35 C. Prentice, J. Morrison, A. D. Smith and E. Zysman-Colman, *Chem. - Eur. J.*, 2023, **29**, e202202998.
36 S. R. Rather and G. D. Scholes, *J. Phys. Chem. A*, 2016, **120**, 6792–6799.
37 Z. Wei, T. Nakamura, S. Takeuchi and T. Tahara, *J. Am. Chem. Soc.*, 2011, **133**, 8205–8210.
38 F. D. Fuller, J. Pan, A. Gelzinis, V. Butkus, S. S. Senlik, D. E. Wilcox, C. F. Yocum, L. Valkunas, D. Abramavicius and J. P. Ogilvie, *Nat. Chem.*, 2014, **6**, 706–711.
39 S. R. Rather, N. P. Weingartz, S. Kromer, F. N. Castellano and L. X. Chen, *Nature*, 2023, **620**, 776–781.
40 Z. Yang, G.-X. Yang, S. Jiang, M. Li, W. Qiu, X. Peng, C. Shen, Y. Gan, K. Liu, D. Li and S.-J. Su, *Adv. Opt. Mater.*, 2023, **12**, 2301711.
41 Y. Song, C. Qin, S. Dong, X. Li, A. Wei, G. Zhang, R. Chen, J. Hu, G. Zeng, L. Xiao and S. Jia, *Laser Photonics Rev.*, 2024, **18**, 2400093.
42 F. Neese, *WIRES Comput. Mol. Sci.*, 2022, **12**, e1606.
43 S. Jiang, J. Lin, D. Li, M. Li, Y. He, W. Xie, J. Chen, Y. Gan, G.-X. Yang, Z. Yang, W. Li and S.-J. Su, *Chem. Eng. J.*, 2023, **452**, 139201.
44 J. Zhang, D. Liu, D. Li, K. Sun, W. Li, Y. Meng, C. Liu, Y. Wu, K. Fang, X. Mu, C. Liu, S. Su and Z. Ge, *Angew. Chem., Int. Ed.*, 2024, **64**, e202415856.
45 M. R. Kennedy, L. A. Burns and C. D. Sherrill, *J. Phys. Chem. A*, 2012, **116**, 11920–11926.
46 W. Wang and P. Hobza, *Chemphyschem*, 2008, **9**, 1003–1009.
47 S. Grimme, *Angew. Chem., Int. Ed.*, 2008, **47**, 3430–3434.
48 S. R. Rather and G. D. Scholes, *J. Am. Chem. Soc.*, 2019, **141**, 708–722.
49 CCDC 2224085: Experimental Crystal Structure Determination, 2025, DOI: 10.5517/ccdc.csd.cc2dnbp3; CCDC 2452457: Experimental Crystal Structure Determination, 2025, DOI: 10.5517/ccdc.csd.cc2n9zjh.